Registration of Liver Images to Minimally Invasive Surface and Subsurface Data

By

Yifei Wu

Thesis

Submitted to the Faculty of the

Graduate School of Vanderbilt University

in partial fulfillment of the requirements

for the degree of

MASTER OF SCIENCE

in

Biomedical Engineering

May, 2014

Nashville, Tennessee

Approved:

Michael I. Miga, Ph.D.

Robert L. Galloway, Ph.D.

ACKNOWLEDGEMENTS

I would like to thank my advisor Dr. Michael Miga for his guidance and Dr. Caleb Rucker for all of his advice and development of the algorithm which forms the basis for this work. I am thankful to Dr. Bob Galloway for his critical insights on writing this thesis. I am also grateful to the rest of the members of the BML and SNARL labs for their friendship and support, particularly Rebekah Conley for her assistance in performing the role of surgeon in my experiments, Tom Pheiffer for his invaluable help in navigating this write-up, Mike Delisi and Dr Galloway for their generous contribution of laparoscopic equipment, Ray Lathrop for developing the conoscopic mounting bracket used in this study and Amber Simpson for coding the conoscope module. I am also thankful for Ramya Balachandran, Wendy Lipscomb, and Dr Labadie for their crucial role in allowing me to get CT of the phantoms, and Jordan Halasz at CELA for supplying the abdominal laparoscopic trainer box.

TABLE OF CONTENTS

LIST OF FIGURES

LIST OF ABBREVIATIONS

Abbreviation	Full Name
1. OR	Operating room
2. LRS	Laser range scanner
3. FEM	Finite element method
4. BC	Boundary conditions
5. (w)ICP	(weighted)iterative closest point
6. TRE	Target registration error
7. PDE	Partial differential equation
8. MRI	Magnetic resonance imaging
9. CT	X-Ray Computed tomography
10. US	Ultrasound

CHAPTER 1

INTRODUCTION

1.1 Motivation

The American Cancer Society estimates that 30,000 new cases of primary liver cancer will occur in 2013in the United States (Howlander 2013). In addition about 35,000 (25%) of those diagnosed with colorectal cancer will present with liver metastasis (Gruenberger 2008). For many, liver cancer is often accompanied by other conditions such as cirrhosis and liver failure. The five year relative survival rate is only about 16% for primary cancer and about 10% for secondary metastasis. Patients with small resectable tumors and without other serious health issues who undergo treatment have much higher survival rates of around 50%.

While chemotherapy can prolong survival, tumor response has been reported to be limited (Fong 2008) and incomplete. Transplants are the best option, but donors are always limited. At present, surgery is one of the few options available that can cure primary liver cancer (ACS 2013). Liver resection, previously considered high risk, is now considered a standard of care due to improvements in safety and studies on efficacy of resections (Grazi 2001).

However, not every patient is a good candidate for surgery. Only about 30% of admitted patients are selected for resection (Manizate 2010). The main considerations for surgery are usually the size of the tumor and its location and the overall health of the liver. The size of the tumors will determine whether resection leaves behind enough functional liver volume for regeneration and function. It is commonly accepted that at least 20% of total liver volume needs to be reserved for otherwise healthy parenchyma. More reserve tissue is needed if the liver is cirrhotic or needs to undergo chemotherapy. The location of the tumor determines whether it can be safely removed without excessive damage to nearby blood vessels. Those tumors near major vessels such as the inferior vena cava may be inoperable due to high risks of massive hemorrhage (Azoulay 2006) and poor safety margins. *To achieve complete resections*

without compromising vasculature or excessive tissue removal requires detailed knowledge of the anatomical relationships involved and spatial skills to resolve the anatomy in an intraoperative setting.

Before an operation, a surgeon usually has preoperative imaging data to allow visualization and localization of the tumor and anatomical landmarks. X-Ray Computed Tomography (CT) and Magnetic Resonance Imaging (MRI) are commonly employed due to their high spatial resolution and contrast. The images are helpful for surgical planning but are often underutilized during a surgery because of the substantive difference in presentation between the preoperative and intraoperative states. In addition, organs shift and non-rigid deformations occur due to mobilization when connective tissue is removed and padding is added thereby changing the support surfaces (Heizmann 2010).

In contrast to preoperative imaging modalities, intraoperative imaging is usually more expensive and potentially cumbersome due to workflow limitations resulting in interference with other surgical equipment. Alternatively, one could use readily-available but spatially incomplete intraoperative localization data and novel registration methods to align preoperative image information to the intraoperative setting. Registration often uses sparsely acquired intraoperative patient localization data (e.g. synthetic fiducial markers adhered to the patient prior to preoperative imaging and available intraoperatively for digitization) to transform the preoperative scan images into the pose as seen in the operating room (OR). A good registration can help the surgeon to quickly and accurately define tumor margins, ultimately improving surgical outcomes.

Jarnagin (2002) performed a multivariate analysis on the predictors of positive outcomes after hepatic resection and concluded that the main factors were number of hepatic segments resected and operative blood loss. In an effort to improve outcomes, many surgeons have now opted to perform a minimally invasive surgery when possible versus a traditional open laparotomy.

Since the Louisville statement (Buell 2008), minimally invasive liver surgery has gained acceptance. The statement was the result of an international meeting amongst hepatobiliary surgeons. The somewhat

contested conclusion of the congress was that "Laparoscopic liver surgery is a safe and effective approach to the management of surgical liver disease in the hands of trained surgeons with experience in hepatobiliary and laparoscopic surgery." In addition to reduced recovery time and trauma, studies suggest that the short and long term outcomes of laparoscopic liver resection (LLR) are comparable to those of open surgery (Vigano 2013). However, compared to open surgery, LLR poses additional challenges to surgeons to achieve the same oncological results. Some problems include reduced field of view, reduced depth of field and inability to palpate tissue. These factors increase the difficulty of following surgical resection plans that ensure negative tumor margins and preserve liver volume and function.

The limitations in visibility increase the value of a surgical navigation system that accurately track and display intraoperative deformation. However, these limitations also apply to the amount and type of registration data that can be collected. The goal of this work is to investigate a method of obtaining intraoperative data in a LLR context and to compare the feasibility of this method to methods used in open liver cases. In simpler terms, we would like to know the accuracy of a registration based on LLR data versus the "bronze standard" of what is obtainable in an open case.

1.2 Previous works

Liver Deformation Registration

A number of groups have worked on liver registration in open cases. Herline (2000) used an optically tracked surgical probe to trace a digital representation of the surface of the liver. A surface registration can then be performed to rigidly align the preoperative model to the swabbed points. Due to the relatively sparseness of features on the liver, the determination of surface correspondence can become an intractable problem without proper initial alignment to constrain the search space. Cash (2005) experimented with a deformation-identifying rigid registration to identify the alignment of the model with respect to the intraoperative pose. Clements (2008) developed a robust method to register images using surface probe data and salient features. By designating anatomic features in the preoperative model and swabbing the

corresponding features using a tracked probe, a weighted patch iterative closest point algorithm can be employed to achieve rigid alignments that are robust to initial poses.

Zijlmans (2012) has found that there can be significant tumor movement in a laparoscopic case. An animal model was used to compare the preoperative images with intraoperative CT images under the effects of heartbeat, respiration, surgical manipulation and pneumoperitoneum. An average shift of 35mm was found and while human anatomy is different, it is predicted that the non-rigid component would be even larger than for pigs due to the relative immobility of the human organ. In an open case clinical study, Heizmann (2010) found that the major deformations were caused by the bedding of the mobilized organ i.e. a change in the posterior support surface. Peterhans (2010) developed a system for open surgery navigation using ultrasound for registration. Using only rigid transformations, they were able to achieve landmark registration errors on the order of 10mm. The results of these studies suggest that there can be improvements to registration by accounting for nonrigid deformations.

Lange (2003) published a study on using b-splines to deform and match preoperative segmented blood vessels to match intraoperative US detected vessels. Their algorithm was able to match about 30 vessel segments with only 1-2 mismatches per patient. Cash (2005) noted that a rigid and a non-rigid registration can be performed sequentially to estimate the intraoperative deformation. In this study, after a landmark rigid registration, the preoperative liver Finite Element Model (FEM) was deformed using boundary conditions created from the intraoperative data and *a priori* knowledge. Dumpuri (2010) investigated the use of a surface Laplacian filter to extrapolate boundary conditions for non-rigid deformation of the liver to fit the surface data. The filter enforces smoothness resulting in deformations that are realistic looking. They report that for phantom studies, the algorithm achieves 3.5 mm or less TRE for 77% of subsurface targets. Rucker (2013) investigated using a posterior displacement to characterize intraoperative deformation. The displacement field on the posterior side was iteratively solved for to obtain boundary conditions that optimized a metric measuring the partial surface fit between the model and the

intraoperative LRS data. The experiments simulated collection of data from open cases and found that the proposed nonrigid algorithm may improve accuracy by up to 44% over the surface Laplacian method.

Intraoperative US

Ultrasound is a comparatively cheap (compared to intraoperative MRI and CT) modality that can collect subsurface data. Commonly, a 2D ultrasound probe in B-mode obtains 2D image slices. If the probe's position and orientation are tracked, this can be used as freehand 3D ultrasound to obtain a volume of subsurface information. 3D probes also exist that can scan a volume (e.g. VOLUSON) but these are far more expensive. Tracked US has previously (Peterhans 2010, Lange 2003) been used as a tool for liver surgery navigation due to its ability to resolve blood vessels and some types of tumors. This technique is used in both open and laparoscopic cases. However, due to the low signal to noise ratio of US images, even manually aligned US to CT images report mean Fiducial Registration Errors (FRE) of ~5 mm (Wein 2008).

Laparoscopic simulation

Nicolau (2005) investigated the feasibility of using tracked instruments in a laparoscopic context. A phantom abdominal setup was used to simulate the laparoscopic setting. Using a simple stereoscopic camera and low cost markers, they were able to achieve tool tip errors of around 1.5mm. The study demonstrates the viability of tracking endoscopic tools in real time with reasonable accuracy.

Conoscope studies

A tracked surgical probe is a simple way to digitize the shape or to designate salient features on the organ surface. Due to deformations induced by probe contact during swabbing, some groups have investigated contactless methods such as Cash (2003) where a laser range-scanner (LRS) was used. In contrast to contact methods, the LRS does not deform the surface and the recorded data reflects the state of the

surface as it is presented. However, the size of the LRS is only suitable for open cases and laparoscopic cases require smaller instruments that can fit through a trocar or at least a hand port.

A conoscope has been proposed as a solution. The conoscope emits a laser beam which is reflected off the measured surface. The reflected light is captured by the conoscope. The resulting interference pattern and phase change is used to calculate the offset distance to the object (Sirat 2005). When tracked, it can be used as a contactless probe with a variable offset. The benefit of using a conoscope is similar to using a LRS-there is no contact deformation when recording the data. However, like the LRS, it suffers from line of sight limitations. In addition, the density of the swabs collected is dependent on the operator. Lathrop (2010) used a conoscope to measure the topography of an animal liver through a narrow trocar and showed that it was feasible for laparoscopic use. They also demonstrated that the conoscope can provide data quality similar to LRS and is suitable for biological tissue. Simpson (2013) compared the performance of using the LRS, conoscope and contact swabbing to register organ surfaces. Surface points from a cadaver kidney and a porcine liver were obtained using the three methods and registered to a model of the organs. The conoscope was shown to perform better than the LRS in terms of surface registration errors and both were better than contact swabbing.

1.3 Contributions

The goal of this work is to investigate the application and extension of a previously studied open abdominal registration framework on laparoscopic cases. The phantom experiments were designed around using a laparoscopic abdominal trainer box to restrict the extent of the surface data collected. The experiments also tested the feasibility of using an optically tracked conoscope to collect swab data. In addition, a phantom mimicking hepatic tissue and vessels was constructed and used for collection of subsurface data. Finally, the liver registration algorithm was extended to incorporate subsurface and surface data in the determination of the optimal registration pose.

CHAPTER 2

METHODOLOGY

2.1 Registration Framework

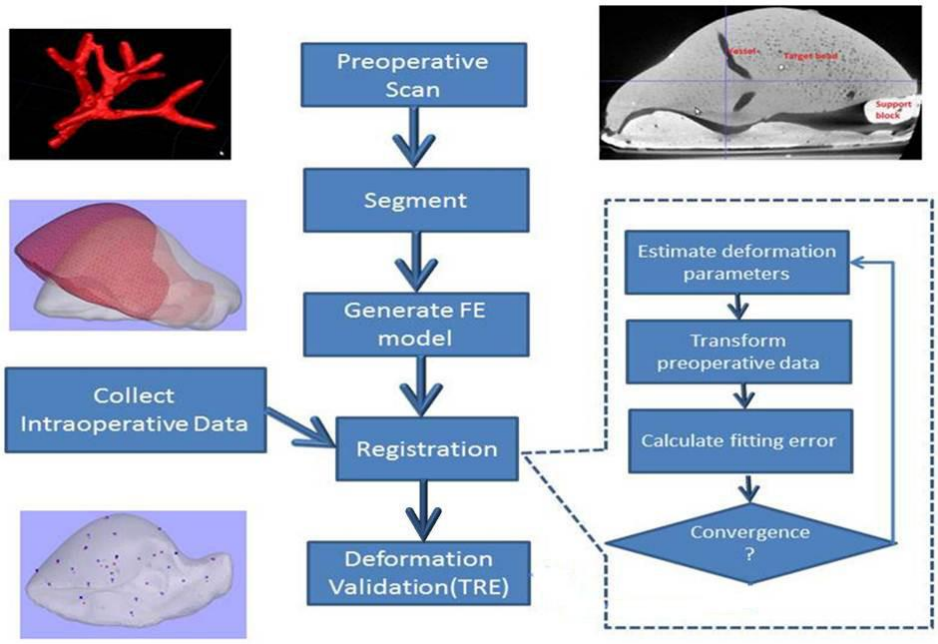

Figure 1 General overview of our registration workflow (dashed box is a call-out covering the iterative steps of the optimization algorithm).

There are 3 major steps involved in the registration workflow. 1) A preoperative tomographic (MR or CT) imaging scan of the relevant organ is segmented and digitized into a soft tissue biomechanical Finite Element (FE) model, 2) a set of sparse intraoperative data is collected from the deformed state and finally, 3) the registration algorithm is used to calculate the displacement field describing how the preoperative model should be deformed to match the intraoperative data. The registration framework used was based off the work of Rucker (2013). Fig. 1 shows an overview of the registration process and the steps are described in more detail below.

Segmentation and generation of a volumetric mesh

In our usual presentations, the liver is imaged by CT to obtain a raw tomogram. The image slices are semi-automatically segmented to obtain a clean representation of the geometry of the organ. The segmented images are converted to a 3D volume using the Marching Cubes algorithm (Lorensen 1987). The volume is filtered using radial basis functions to reduce surface noise. A custom-built mesh generator algorithm based on Sullivan (1997) is used to create the tetrahedral elements for the 3D finite element models. An image-to-grid material property designation process can then be executed to assign material properties to different tissue types. In the work herein however, a homogeneous organ was assumed.

Intraoperative data acquisition

Sparse data about the deformed intraoperative state is captured to drive the registration. Surface and subsurface information is collected from the deformed intraoperative state of the organ. The surface topography is acquired as a digitized point cloud representation using tracked conoscope noncontact swabs. The subsurface information can be acquired through tracked intraoperative ultrasound. The US images can then be segmented to produce point cloud representations of the vessel structures. In the work herein, US subsurface features were simulated using partial volumetric subsurface CT data.

Rigid Registration

Anatomical features are designated on the preoperative images and corresponding landmarks are obtained from the intraoperative state. An initial alignment between the model and the intraoperative data is made by using the weighted salient anatomical feature algorithm previously described by Clements (2008).

2.2 Non-rigid Deformation Modeling

A Priori, we assume that the majority of deformation is induced by changes in the support surface on the posterior of the liver. The liver is often propped up by surgical towels for presentation in open cases, and by laparoscopy pads in LLR cases. Thus the assumed main modes of deformation are induced by a

change in the posterior surface. The displacements (Type I, Dirichlet boundary conditions) are parameterized by a loading function in the form of a bivariate 3rd degree polynomial that prescribed nodal displacements in the direction of the mean normal direction of the posterior surface (Equation 1).

1) $$u = \hat{n} \sum_{1 \le i+j \le n}^{n} c_{ij} t_1^i t_2^j$$

$\boldsymbol{u}$ represents the nodal displacement vector

$\hat{\boldsymbol{n}}$ represents the unit vector of the mean normal direction of the posterior surface

$\boldsymbol{t_1}$ and $\boldsymbol{t_2}$ represent the tangential coordinates of the node

$\boldsymbol{c}$ represents the polynomial coefficients

$\boldsymbol{n}$ is the highest polynomial degree of the displacement field

$\boldsymbol{i}$ and $\boldsymbol{j}$ represent exponents. The summation is used to exclude redundant rigid rotational modes

The boundary nodes on the posterior (painted red in Fig 2) were defined to have these Type-I Dirichlet loading conditions while the other nodes were defined to be stress free.

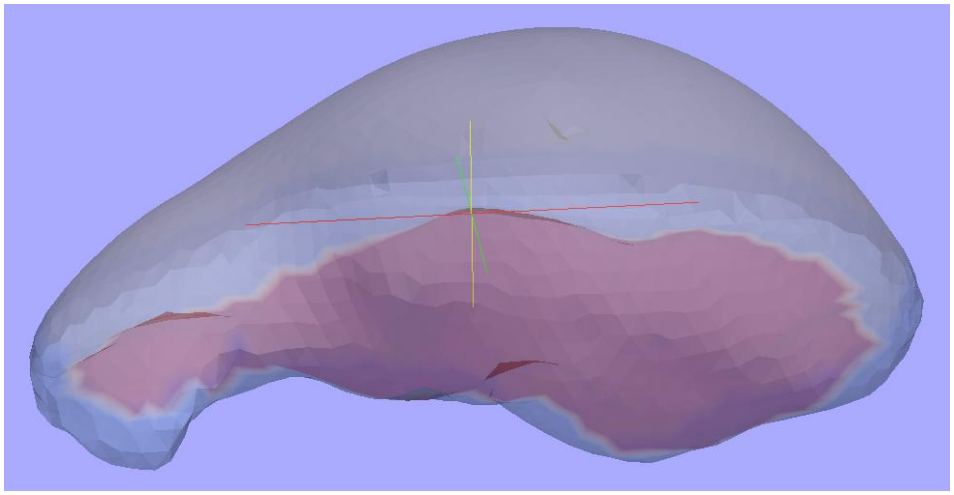

Figure 2 Liver posterior support surface (red)

Once our loading function is defined, and subsequent boundary conditions are deployed, the 3D Navier-Cauchy equations are used for describing the remaining volumetric displacement field:

2) $$\frac{E}{2(1+\nu)(1-2\nu)}\nabla(\nabla \cdot u) + \frac{E}{2(1+\nu)}\nabla^2 u + F = 0$$

E is the elastic modulus

v is the Poisson's ratio

u is the displacement vector

F is the body force distribution

In this case, no body force distribution is prescribed and deformation is induced purely by boundary condition effects. The partial differential equations are solved using the Galerkin weighted residual method using the standard C^o continuous linear basis function associated with tetrahedral elements. Once assembled, a system of equations in the form of Equation 3 is generated and the global displacements are solved using sparse matrix methods.

3) $$[K]\{u\} = \{f\}$$

[K] is the stiffness matrix

{u} is the nodal displacements vector

{f} is the forcing function vector

A Jacobian of the global model reflecting changes in the node displacements response to changes in the coefficients of the loading polynomial was created using a finite difference approach (Equation 4). Assuming linearity of the model, the principle of superposition allows quick calculation of nodal displacements by using any linear combination of loading coefficients.

4) $$J(\beta) = \begin{bmatrix} \frac{\delta u_1}{\delta \beta_1} & \cdots & \frac{\delta u_1}{\delta \beta_m} \\ \vdots & \ddots & \vdots \\ \frac{\delta u_n}{\delta \beta_1} & \cdots & \frac{\delta u_n}{\delta \beta_m} \end{bmatrix}$$

β is the set of coefficients of the loading function Eq 1.

u is the set of nodal displacements

n is the number nodes in the FE model

m is the number of coefficients in our loading function

2.3 Registration Algorithm

The registration algorithm minimizes an objective function that measures the misfit between the preoperative model and the intraoperative surface/subsurface points. The objective function is calculated as follows:

$$5) \qquad G(\Psi) = \frac{1}{N}\sum_{i=1}^{N}\left(\hat{n}_{ci}^{T}(p_{di} - p_{ci})\right)^2 + \alpha_1 U^2 + \sum_{j=1}^{M}\alpha_2 \left\|p_{dj} - p_{cj}\right\|^2$$

$$6) \qquad U = u^T K u$$

$$7) \qquad \Psi = \left\{\bar{c}, t_x, t_y, t_z, \theta_x, \theta_y, \theta_z\right\}$$

N is the number of surface points collected intraoperatively

M is the number of subsurface intraoperative points

$\hat{\boldsymbol{n}}_{\boldsymbol{ci}}$ is the unit normal vector to the model surface at point p_{ci}

$\boldsymbol{p}_{\boldsymbol{di}}$ are the coordinates of the surface point cloud

$\boldsymbol{p}_{\boldsymbol{ci}}$ are the coordinates of the corresponding model surface node

$\boldsymbol{\alpha}_{\boldsymbol{1}}$ is a smoothness constraint scaling constant

U is the total energy stored in the nonrigid displacement field and is defined by equation 6

u and ***K*** represent the displacement vector and the stiffness matrix respectively

$\boldsymbol{\alpha}_{\boldsymbol{2}}$ is a scaling constant to adjust the relative contribution of the subsurface points to the objective

$\boldsymbol{p}_{\boldsymbol{sj}}$ is the coordinates of the subsurface point cloud

$\boldsymbol{p}_{\boldsymbol{dj}}$ is the coordinates of the corresponding model subsurface node

The coefficients of the posterior displacement polynomial, the translations associated with rigid spatial alignment and the angles associated with rigid rotation, constitute the optimization parameter set,Ψ, as defined in equation 7. The rigid alignment is used as an initialization pose. The Levenberg-Marquardt algorithm was used to iteratively optimize the parameter set that estimates the deformation that best fits the intraoperative data. Correspondence is assigned by closest point correspondence-- intraoperative and

preoperative points of the current estimated deformation are assumed to correspond if they are the closest neighbors. Note that the correspondences are considered to be soft-assigned and are recalculated for each iteration. When available, subsurface points are used in the objective function (Equation 5) to measure the misfit between the intraoperative subsurface and the model subsurface.

2.4 Phantom Design

The phantom was made similar to the one described in Rucker (2013). Briefly, an Ecoflex(Smooth-On, Easton PA) silicone phantom in the shape of a human liver was cast with embedded surface and subsurface targets. A total of 29 CT-opaque target beads were implanted to track the displacement of the liver to validate the calculated displacement field from the model. In addition, vessels were simulated by inserting wax vessels into the portal triad area. These simulate large vessels such as the biliary tree or the hepatic portal vein that are commonly visible in US imaging. After casting, the wax was removed by heating and melting a-la lost wax casting. The diameter sizes of the vessels are on the order of larger vessels found in human livers (Conversano 2011). The diameter of the main segments was ~10mm and the smallest subsegment was ~4mm.

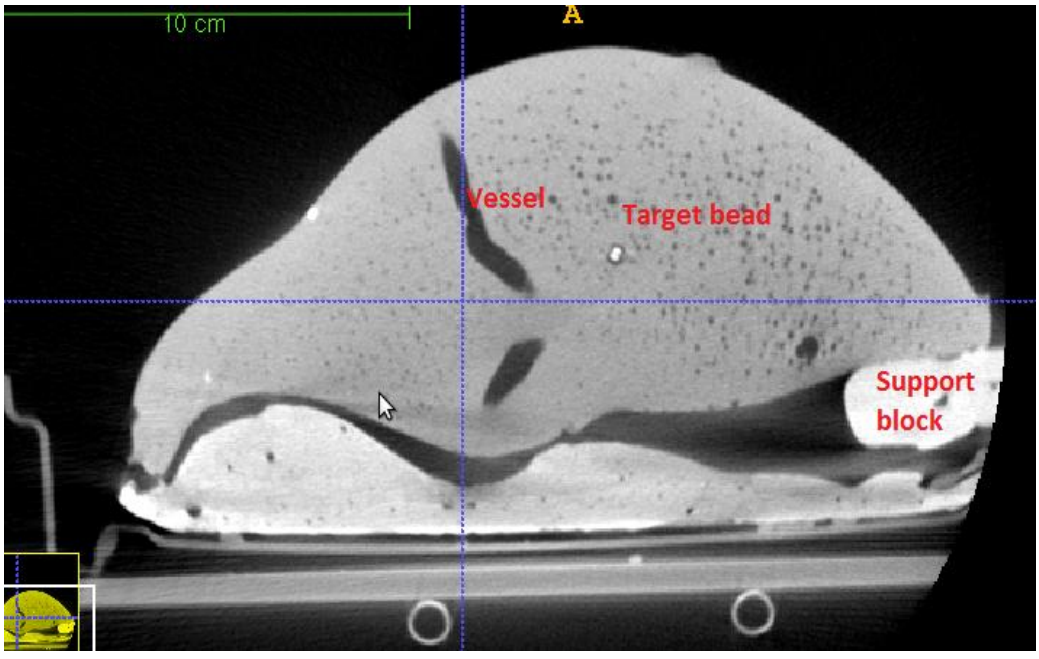

Figure 3 Phantom CT slice

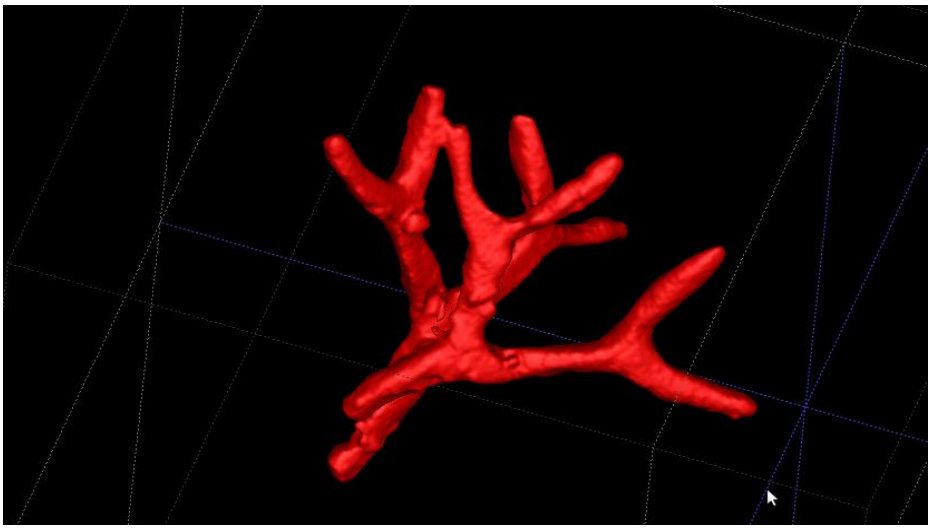

Figure 4 Segmented vessels in liver phantom

2.5 Phantom Experiments

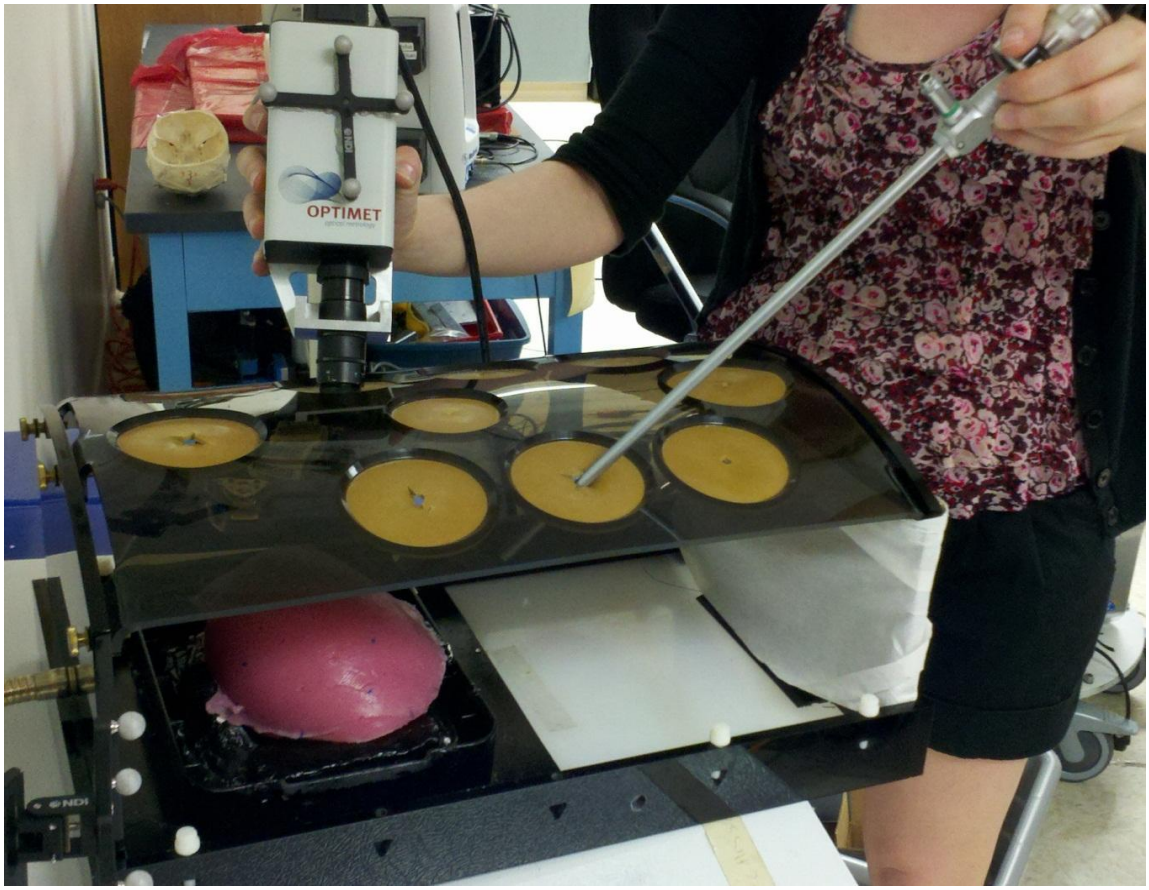

Figure 5 Experimental Setup

A set of phantom experiments were performed to simulate the type of data that can be collected in an LLR case. An abdomen laparoscopy trainer box (Karl Storz, Tuttlingen Germany) was used to constrain and simulate the physical limitations of laparoscopic ports. The phantom had 8 access ports to allow laparoscopic tools access to the cavity. For the purpose of the experiment, 3 ports were used for data collection. The three ports that were used are similar to actual port placements (Fong 2000) as seen in Fig 6. The distance between the "abdomen wall" and the surface of the liver was approximately 10-15cm as common for standard normal insufflation pressures of 10-14mmHg.

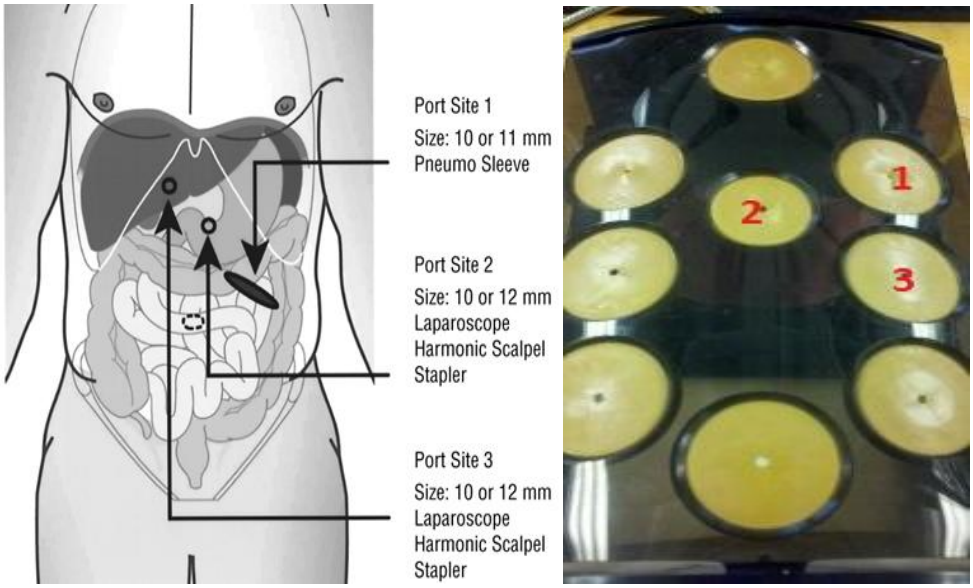

Figure 6 Left: Port locations from Fong (2000), Right: Port designations for experiment

2.6 Data Collection

First a reference "mock preoperative" CT scan was taken. This represents the state of the undeformed organ before the surgery. Then, intraoperative deformations were simulated by adding solid blocks to change the support surface on the posterior (Fig 3). For each deformed pose, surface data was recorded through three different ports using the conoscope. After collection, a CT of the deformed state was taken to establish the true location of the target beads and to obtain the true deformed geometry. Subsurface and

large surface extent data was retrospectively obtained from segmenting the deformed state CT. A total of three different poses were induced to represent variations in clinical presentation. .

Conoscopic measurements

An Optimet Mark 10 conoscope (Jerusalem, Israel) was used to digitize the phantom surface into point cloud data. The conoscope was mounted to a custom-built bracket with passive optical markers mounted on a rigid body. A NDI Polaris (Waterloo, Canada) camera was used to track the position of the bracket. The data collection system was calibrated to map the distance offset of the conoscope into a 3D point coordinate by a pivot calibration (Burgner 2012).

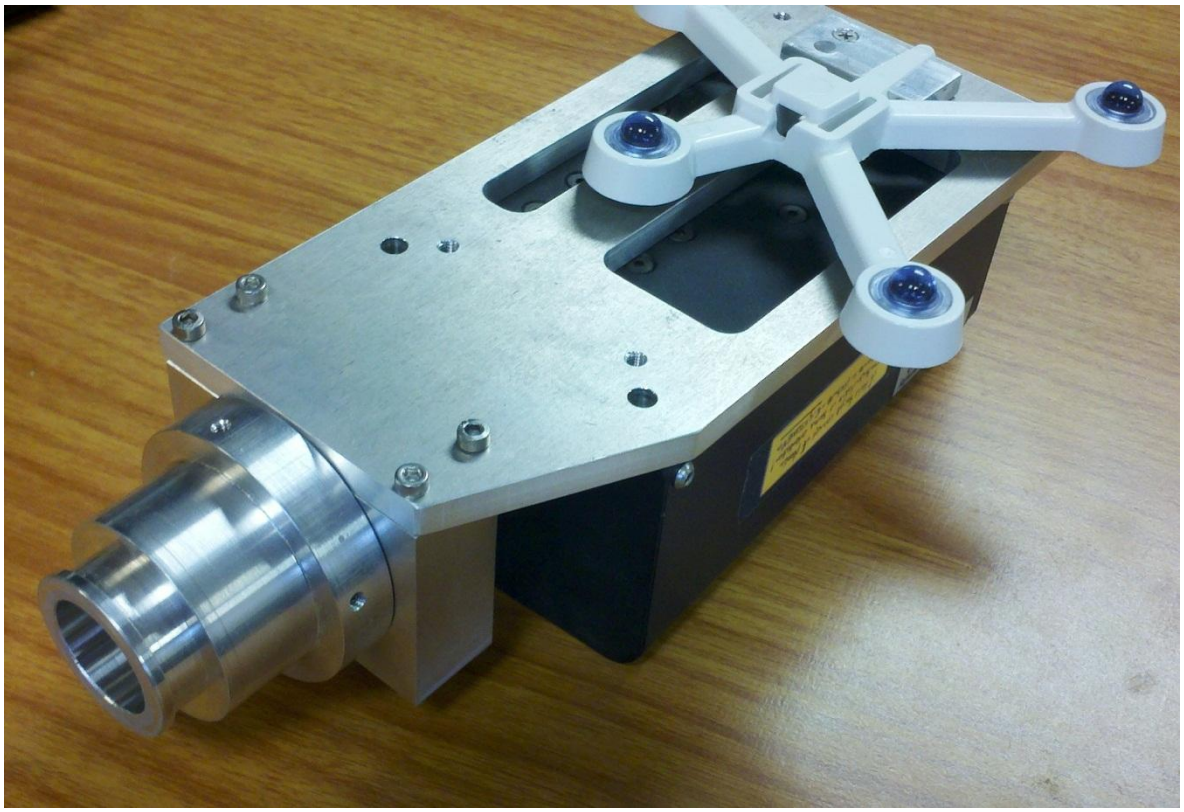

Figure 7 A new prototype of the conoscope mount design with considerations for intraoperative sterility

The calibration resolves the transformation of the conoscope beam direction and origin to the orientation of the tracked rigid body. A laparoscopic tube extension was attached onto the bracket near the laser aperture to allow entry into a laparoscopic port. In a clinical case, the tube would need to fit through a

trocar that acts as an airtight barrier for the pneumoperitoneum. Salient feature swabs were obtained followed by general surface points as permitted by the constraints of the port. In addition to the individual port swabs, an "appended" set was also created by assembling nonredundant surface points from all 3 ports combined. This represents a best-case data collection scenario rarely achieved due to the need for additional ports and increased swabbing time.

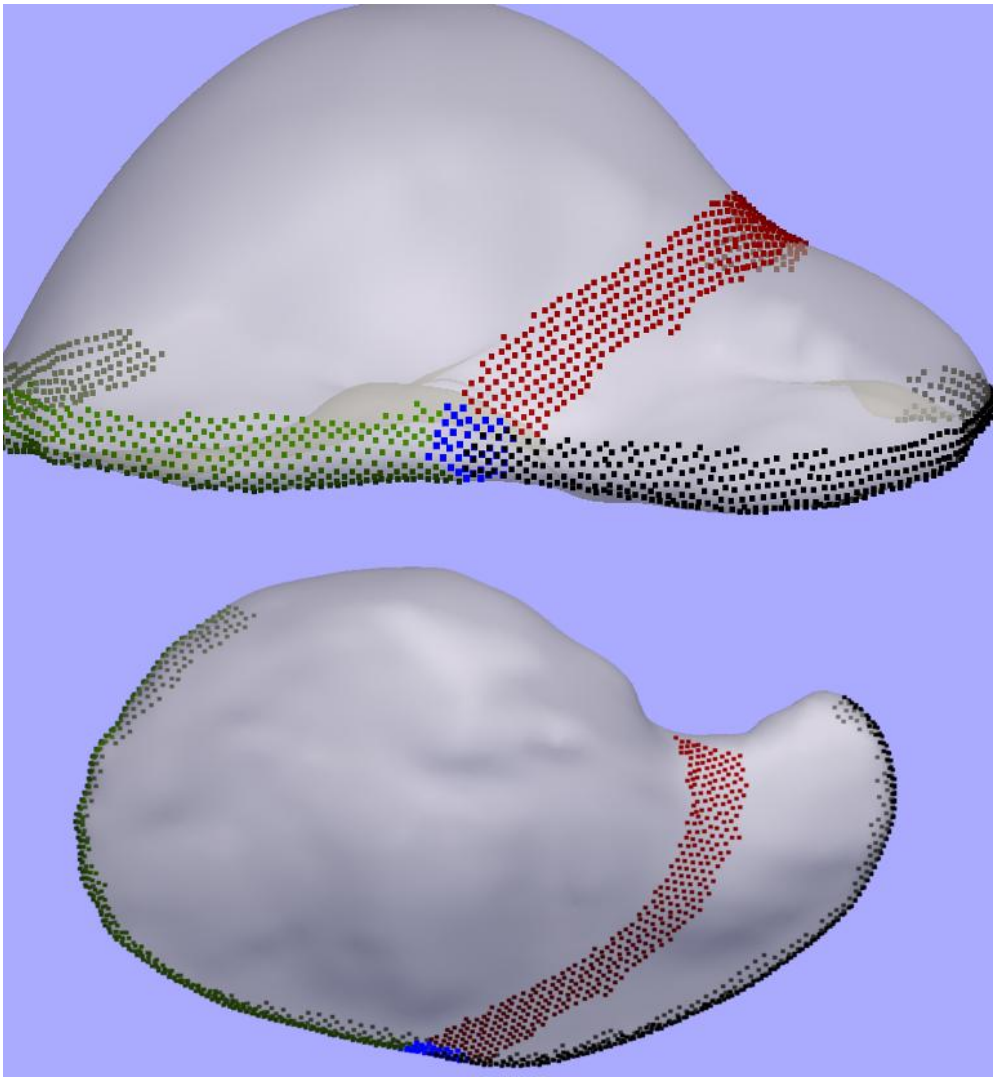

Figure 8 Salient features: Green-right inferior ridge, red-falciform, blue-round ligament, black-left inferior ridge

Simulated LRS coverage

Laser Range Scanner data was simulated by using the segmented CT volume. A patch of anterior surface points with extent similar to what is observed in clinical cases was extracted and downsampled to a 2mm interpoint distance density to reduce computational time in registration.

Subsurface data

Subsurface data was obtained by segmenting the CT volume for the vascular structures. ITK-snap was used to manually designate the vessel regions and the complete vessel boundaries were obtained by using the snake algorithm. The seeds for the snake were designated from the lumen of the vessels. The segmented vessel walls were represented by sets of point clouds. The preoperative segmentation represents what would be obtained in a preoperative CT or CT angiography scan. The points that make up the vessel were down sampled to a 2mm interpoint distance density and constitute a cloud of ~1000 points. The vessel points that represent the intraoperative subsurface data were downsampled to a 5mm interpoint distance density resulting in a point set containing ~150 points. The sparseness of the intraoperative data is intended to reflect the coarse resolution from freehand ultrasound. The extent of each of the different datasets is illustrated in Fig. 9B.

2.7 Validation and Target Registration Error Calculations

The accuracy of our registration was evaluated by the comparing the displacement field predicted by our registration to the actual displacement field of the deformed organ. Target beads embedded in the phantom are used to track the surface and subsurface displacements. The preoperative scan was used to establish the starting positions of the beads and the intraoperative CT was taken after each of the deformations to determine the true displacement of the corresponding beads. From the registration, the intraoperative bead displacements are predicted based on the displacement field from the deformed model. The preoperative to intraoperative marker displacement vector is assumed to be the same as the

displacement vector for the closest node. Finally, to calculate the mean target error, the Euclidean distances between the predicted and true positions are calculated and we report the root mean square of the target error vector (TRE).

CHAPTER 3

RESULTS

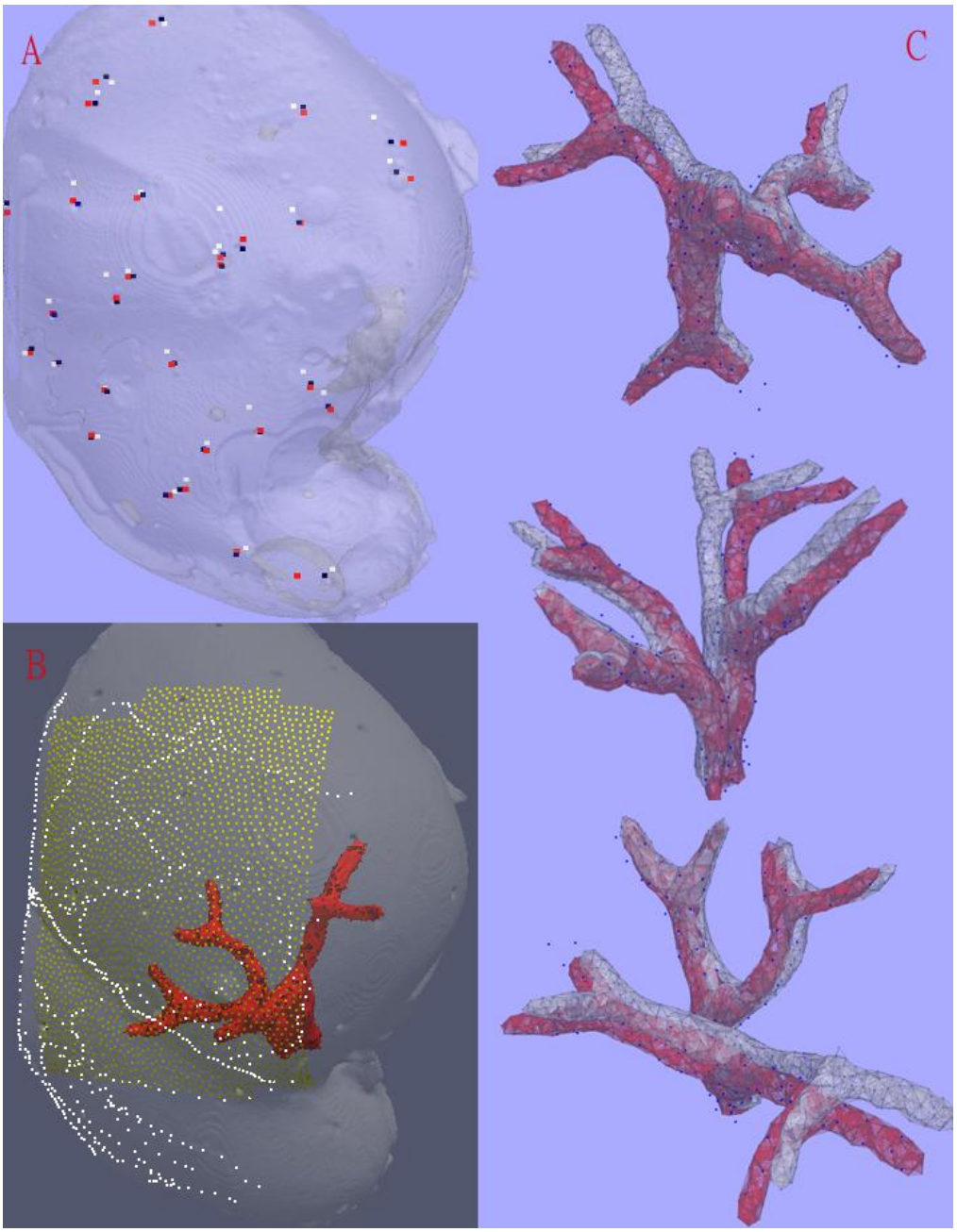

Figure 9 A: Bead locations after registration--blue represents the true intraoperative locations and red represents the model predicted locations, white represents rigid registration results. **B**: Spatial extents and density of the data sets used. White represents the conoscope feature and surface swabs, yellow shows the LRS surface cloud and red represents the preoperative vessels. **C**: Vessels before and after registration. The blue represents the true intraoperative vessel wall after down sampling to simulate US sparseness. The red represents the nonrigidly registered preoperative vessel. The white represents the preoperative vessel rigidly registered.

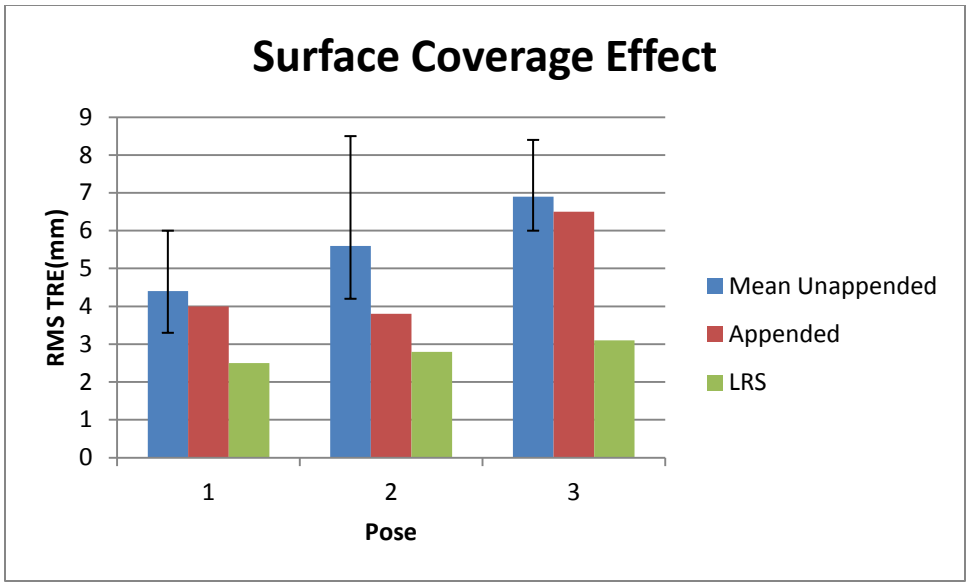

Figure 10 Registration TRE for combined port data. Error bars represent the high and low mean TRE of the set of unappended conoscopic data. The appended set combines the surface swabs from all three ports. The LRS set is a large subpatch of the anterior surface.

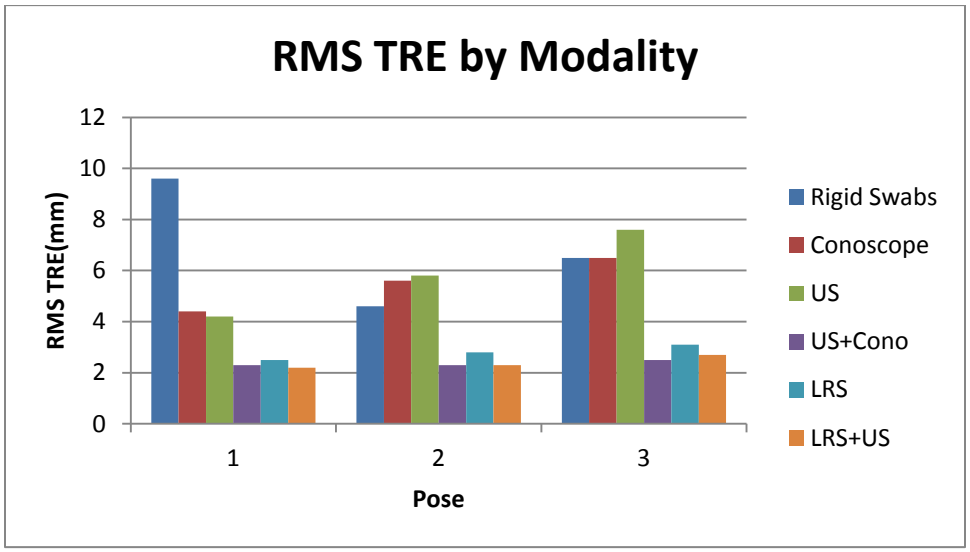

Figure 11 Effects of Different Modalities. This figure compares the accuracy of using different amounts/types of data in the nonrigid registration. 'Cono' represents the registration using the conoscope surface data. 'US' uses only subsurface vessel wall points. 'US+cono' uses both surface and subsurface points. 'LRS' uses a large extent surface patch and 'LRS+US' uses both the large surface patch data and subsurface information. Rigid swabs represent the baseline initial pose after the rigid registration step using salient feature swabs taken with the conoscope.

	Rigid	Cono	US	LRS	Cono+US	LRS+US
Mean TRE(mm)	6.9	4.767	5.867	2.8	2.367	2.4
SD	2.524	1.504	1.701	0.3	0.1155	0.2646

Figure 12 Summary of the registration results in Fig 11 from all three poses.

3.1 Qualitative Registration Accuracy (Figure 9)

The results were visualized to assess the quality of the registrations. Fig. 9A depicts the registration results from one of the poses. The true location of the target beads are shown along with the predicted locations based on a rigid swab registration and a nonrigid registration using both conoscope swabs and ultrasound data. Note that the predicted bead locations look aligned with the true bead locations and there were no unaccounted for or unmatched beads.

The registrations were also judged by the fit of the deformed vessel wall to the intraoperative subsurface data (Fig 9C). The registration performance seems reasonable since most of the deformed points match up to the vessel walls. It is also worth noting that the deformed points remain structurally similar to the preoperative model. In addition the rigid registration produced non-negligible mismatch to the true pose illustrating the amount of nonrigid deformations induced.

3.2 Quantitative Results (Figures 10-12)

Comparing the low surface coverage data with the larger surface coverage data (Fig. 10), there is a correlation that suggests increasing the density and the extents of the surface data can improve registration accuracy. In all cases, the registrations using LRS outperforms the registrations using only conoscope data. However, using combined conoscope swab points from three ports does not seem significantly better than using only one port.

Fig. 11 compares the registration results of using various surface data and when subsurface data was used in conjunction with the surface data. 'Rigid swabs' represents results after a rigid registration using conoscope swabbed salient features. This initialization serves as a baseline starting point for all subsequent nonrigid registration. Nonrigid registrations using only conoscope surface swabs and the registrations using only subsurface data had accuracy similar to those obtained from a rigid registration. When subsurface and surface datasets were used together (Cono+US), the results were improved and similar to registrations using large surface coverage (LRS). Using subsurface information with the large

surface extent data to register (LRS+US) did not seem to add further improvement as compared to just using LRS.

Assuming normal distribution of errors, an ANOVA test was used to see if there was a difference between the various groups. The results were affirmative, and a set of post tests were performed to show which groups were significantly different from each other. The post-tests accounted for multiple comparisons by using the conservative Bonferroni correction factor or the more powerful Newman-Keuls test which only compares the groups with the most differing means. The post-tests using Bonferroni suggested that the Cono+US and the LRS+US registrations were significantly different from the rigid registration. The less conservative Newman-Keuls correction indicated that in addition to the Cono+US and the LRS+US, the LRS registration was also significantly different from the rigid registration. The tests consider neither the nonrigid registrations using only conoscope swabs nor the nonrigid registrations using only US data to be significantly different from a rigid registration.

CHAPTER 4

DISCUSSION

4.1 Localization Errors

In general, LRS technology can resolve geometric surfaces to submillimetric error and when tracked can localize targets to 2.2 +/- 1.0 mm at ranges appropriate with surgery (Pheiffer 2012). Polaris localization errors with passive targets are on the order of 1-1.5mm (Wiles 2004) and vary depending on location within the viewing volume. The CT images obtained had voxel sizes of 0.4mm.

The target beads were segmented manually from the images using ITK-snap. The beads are ~3mm in diameter and the centers of the beads were picked as the target locations. Three operators independently segmented 29 markers and the extracted marker centers were compared. The sum squared error distance between the 3 sets was submillimetric. An intrasubject trial was also performed with one subject segmenting the same set 4 times. The resulting error was submillimetric as well.

4.2 Appropriateness of Model

The model used makes a few key assumptions. A linear model is used in this study to predict the displacement field of the phantom. This assumption is appropriate for small strain but a larger deformation would necessitate the need to account for the nonlinearity of strain via a full Lagrangian formulation. In addition, we also assume that the FE mesh is a homogeneous solid even though there are "vessels" filled with air within. A more accurate model would define the vessel elements with different material properties and perhaps account for the interface boundary conditions. Finally, we assume that the loading function is appropriate to replicate the deformation conditions. In this case, the liver posterior was displaced in the mean normal direction to the posterior surface without any tangential displacements. The degree of the loading polynomial function defines a level of smoothness for the loading function which limits the spatial frequency/resolution of possible displacements. The loading smoothness needs to match

the appropriate level of deformation seen in surgery while having enough degrees of freedom to match the intraoperative state.

To assess these assumptions we must consider whether or not this model is capable of predicting the deformations that occur. The TRE magnitude is a result of both the model capabilities and the uncertainty in the point correspondences. Assuming we had perfect correspondence, the remaining TRE should be due to model (in)capability of matching the data. To test this, the objective function was set to minimize the sum squared error of the target mismatches i.e. using the target bead locations as input intraoperative data. The average TRE from this registration was 1.5mm. This data represents an incomplete but correct correspondence set of nodal displacements and it sets an upper bound on the size of the model capability errors.

4.3 Surgical Correctness

The placement of laparoscopic ports is challenging due to variations in internal anatomy with relation to external features. Currently, ports are placed based on external features (Feurstein 2008) to roughly allow access to the volume of interest. Thus, it is very difficult to obtain a data set representative of all laparoscopic cases. Regardless, due to the mobility of the organ, it is usually possible for a surgeon to present the organ in a manner such that the anterior surface is accessible to swabbing. We can assume that this set is a reasonable representation of data collected in the OR.

4.4 Effect of increasing surface data coverage/density

In this study we looked at the effect of constraining the datasets to what can be collected by using the conoscope as limited by the abdomen ports. Intuitively, it seems that the open cases have better registration quality simply because of increased extents afforded by the larger opening. The results from the LRS coverage versus conoscope port coverage suggest that the larger spatial extents and density of the simulated LRS dataset lead to better registration. Interestingly, when port data from all 3 ports were combined and used for registration, we did not always see improvement over the best case out of the 3

contributing, but the appended set always improved over the worse. Overall, this suggests that increasing coverage extents and density can help registration quality.

4.5 Effect of adding subsurface data

The results of the ANOVA post-tests suggest that the nonrigid registrations using smaller surface and subsurface information are comparable to the registrations using larger surface extent datasets. Adding ultrasound data to the intraoperative data set seems to help registration quality. Performing a nonrigid registration using only the ultrasound data did not appear to improve accuracy beyond that of the rigid registration probably due to poor initial correspondence assumptions or limited extents. However, when subsurface data is factored in for the LRS and the conoscope swabbed data sets, the mean TRE is improved. This suggests that the subsurface data can provide complementary information to the sparse surface data.

CHAPTER 5

CONCLUSIONS

By looking at the predicted displacements to the true displacements within the phantom, we see there are significant nonrigid deformations unaccounted for by a simple rigid registration. However, applying our nonrigid deformation model does not always help if the correspondence estimation is poor. In the scenario of limited data such as using only surface swabs in a laparoscopic case, the chances of poor correspondence is high and we see that there is a drawback to making the deformation look realistic versus making it accurate i.e. the non-rigidly deformed model looks more realistic but does not increase model accuracy. Sufficient constraints are needed in order for the nonrigid registration algorithm to improve accuracy over the rigid. Once more data is available, such as in an open case demonstrated by our simulated LRS, the increased constraints can cause the non-rigid registration to contribute to increased accuracy. In the case of LLR, the use of subsurface US data in addition to surface swabs showed increased accuracy compared to using either dataset alone. The nonrigid registrations using this composite dataset also consistently improved over the rigid registration results suggesting the increased constraints may justify the use of the nonrigid registration.

The future work I envision would address some of the more advanced methods of deforming the liver and ways to model data error. There might be additional shear or stretch modes that are significant as well as imposed anterior displacements due to the mobilization process. A different set of loading functions may provide more accurate and realistic posterior deformations. The results from this study suggest that the type of intraoperative data collected can influence registration results. The exact relationship between data and TRE quality is still however, not well defined. A preliminary set of analysis tests suggest that there is a minimum surface coverage density threshold below which registrations perform much poorly. A more complete analysis is planned for the near future.

REFERENCES

American Cancer Society. (2013). Liver Cancer Surgery. Retrieved June 13, 2013 from http://www.cancer.org/cancer/livercancer/detailedguide/liver-cancer-treating-surgery

Azoulay, D., Andreani, P., Maggi, U., Salloum, C., Perdigao, F., Sebagh, M., ... & Castaing, D. (2006). Combined liver resection and reconstruction of the supra-renal vena cava: the Paul Brousse experience. *Annals of surgery*, 244(1), 80.

Buell, J. F., Cherqui, D., Geller, D. A., O'Rourke, N., Iannitti, D., Dagher, I., ... & Chari, R. S. (2009). The international position on laparoscopic liver surgery: The Louisville Statement, 2008. *Annals of surgery*, *250*(5), 825-830.

Burgner, J., Simpson, A. L., Fitzpatrick, J. M., Lathrop, R. A., Herrell, S. D., Miga, M. I., & Webster, R. J. (2012). A study on the theoretical and practical accuracy of conoscopic holography-based surface measurements: toward image registration in minimally invasive surgery. *The International Journal of Medical Robotics and Computer Assisted Surgery*.

Cash, D. M., Sinha, T. K., Chapman, W. C., Terawaki, H., Dawant, B. M., Galloway, R. L., & Miga, M. I. (2003). Incorporation of a laser range scanner into image-guided liver surgery: Surface acquisition, registration, and tracking. *Medical Physics*, *30*, 1671.

Cash, D. M., Miga, M. I., Sinha, T. K., Galloway, R. L., & Chapman, W. C. (2005). Compensating for intraoperative soft-tissue deformations using incomplete surface data and finite elements. *Medical Imaging, IEEE Transactions on*, *24*(11), 1479-1491.

Clements, L. W., Chapman, W. C., Dawant, B. M., Galloway Jr, R. L., & Miga, M. I. (2008). Robust surface registration using salient anatomical features for image-guided liver surgery: Algorithm and validation. *Medical Physics*, *35*, 2528.

Conversano, F., Franchini, R., Demitri, C., Massoptier, L., Montagna, F., Maffezzoli, A., ... & Casciaro, S. (2011). Hepatic vessel segmentation for 3D planning of liver surgery: experimental evaluation of a new fully automatic algorithm. *Academic Radiology*, *18*(4), 461-470.

Dumpuri, P., Clements, L. W., Dawant, B. M., & Miga, M. I. (2010). Model-updated image-guided liver surgery: preliminary results using surface characterization. *Progress in biophysics and molecular biology*, *103*(2), 197-207.

Feuerstein, M., Mussack, T., Heining, S. M., & Navab, N. (2008). Intraoperative laparoscope augmentation for port placement and resection planning in minimally invasive liver resection. *Medical Imaging, IEEE Transactions on*,*27*(3), 355-369.

Fong, M. D. (2000). A prospective analysis of staging laparoscopy in patients with primary and secondary hepatobiliary malignancies. *Journal of Gastrointestinal Surgery*, *4*(1), 34-43.

Fong, Y., Jarnagin, W., Conlon, K. C., DeMatteo, R., Dougherty, E., & Blumgart, L. H. (2000). Hand-assisted laparoscopic liver resection: lessons from an initial experience. *Archives of Surgery*, *135*(7), 854.

Fong, Y. (2008). Surgical Therapy of Hepatic Colorectal Metastasis. *CA: A Cancer Journal for Clinicians* 49(4): 231-255.

Grazi, G. L., Ercolani, G., Pierangeli, F., Del Gaudio, M., Cescon, M., Cavallari, A., & Mazziotti, A. (2001). Improved results of liver resection for hepatocellular carcinoma on cirrhosis give the procedure added value. *Annals of surgery*,*234*(1), 71.

Gruenberger, B., Tamandl, D., Schueller, J., Scheithauer, W., Zielinski, C., Herbst, F., & Gruenberger, T. (2008). Bevacizumab, capecitabine, and oxaliplatin as neoadjuvant therapy for patients with potentially curable metastatic colorectal cancer. *Journal of clinical oncology*, *26*(11), 1830-1835.

Heizmann, O., Zidowitz, S., Bourquain, H., Potthast, S., Peitgen, H. O., Oertli, D., & Kettelhack, C. (2010). Assessment of intraoperative liver deformation during hepatic resection: prospective clinical study. *World journal of surgery*,*34*(8), 1887-1893.

Herline, A. J., Herring, J. L., Stefansic, J. D., Chapman, W. C., Galloway, R. L., & Dawant, B. M. (2000). Surface registration for use in interactive, image-guided liver surgery. *Computer Aided Surgery*, *5*(1), 11-17.

Howlader N, Noone AM, Krapcho M, Garshell J, Neyman N, Altekruse SF, Kosary CL, Yu M, Ruhl J, Tatalovich Z, Cho H, Mariotto A, Lewis DR, Chen HS, Feuer EJ, Cronin KA (eds). SEER Cancer Statistics Review, 1975-2010, National Cancer Institute. Bethesda, MD, http://seer.cancer.gov/csr/1975_2010/, based on November 2012 SEER data submission, posted to the SEER web site, April 2013.

Jarnagin, W. R., Bodniewicz, J., Ellen Dougherty RN, M. A., Kevin Conlon, M. D., Blumgart, L. H., & Yuman Fong, M. D. (2000). A prospective analysis of staging laparoscopy in patients with primary and secondary hepatobiliary malignancies. *Journal of Gastrointestinal Surgery*, *4*(1), 34-43.

Lorensen, W. E., & Cline, H. E. (1987, August). Marching cubes: A high resolution 3D surface construction algorithm. In *ACM Siggraph Computer Graphics* (Vol. 21, No. 4, pp. 163-169). ACM.

Lange, T., Eulenstein, S., Hünerbein, M., & Schlag, P. M. (2003). Vessel-based non-rigid registration of MR/CT and 3D ultrasound for navigation in liver surgery. *Computer Aided Surgery*, *8*(5), 228-240.

Lathrop, R. A., Hackworth, D. M., & Webster, R. J. (2010). Minimally invasive holographic surface scanning for soft-tissue image registration. *Biomedical Engineering, IEEE Transactions on*, *57*(6), 1497-1506.

Nicolau, S. A., Goffin, L., & Soler, L. (2005, November). A low cost and accurate guidance system for laparoscopic surgery: Validation on an abdominal phantom. In *Proceedings of the ACM symposium on Virtual reality software and technology* (pp. 124-133). ACM.

Manizate, F., Hiotis, S. P., Labow, D., Roayaie, S., & Schwartz, M. (2010). Liver functional reserve estimation: state of the art and relevance to local treatments. *Oncology*, *78*(Suppl. 1), 131-134.

Peterhans, M., vom Berg, A., Dagon, B., Inderbitzin, D., Baur, C., Candinas, D., & Weber, S. (2011). A navigation system for open liver surgery: design, workflow and first clinical applications. *The International Journal of Medical Robotics and Computer Assisted Surgery*, *7*(1), 7-16.

Rucker, D. C., Wu, Y., Ondrake, J. E., Pheiffer, T. S., Simpson, A. L., & Miga, M. I. (2013, March). Nonrigid liver registration for image-guided surgery using partial surface data: a novel iterative approach. In *SPIE Medical Imaging* (pp. 86710B-86710B). International Society for Optics and Photonics.

Pheiffer, T. S., Simpson, A. L., Lennon, B., Thompson, R. C., & Miga, M. I. (2012). Design and evaluation of an optically-tracked single-CCD laser range scanner. *Medical physics*, *39*(2), 636-642.

Simpson, A. L., Burgner, J., Glisson, C. L., Herrell, S. D., Ma, B., Pheiffer, T. S., ... & Miga, M. I. (2013). Comparison study of intraoperative surface acquisition methods for surgical navigation. *Biomedical Engineering, IEEE Transactions on*, *60*(4), 1090-1099.

Sullivan, J. M., Charron, G., & Paulsen, K. D. (1997). A three-dimensional mesh generator for arbitrary multiple material domains. *Finite Elements in Analysis and Design*, 25(3), 219-241.

Viganò, L., Ferrero, A., Amisano, M., Russolillo, N., & Capussotti, L. (2013). Comparison of laparoscopic and open intraoperative ultrasonography for staging liver tumours. *British Journal of Surgery*, 535-542.

Wein, W., Brunke, S., Khamene, A., Callstrom, M. R., & Navab, N. (2008). Automatic CT-ultrasound registration for diagnostic imaging and image-guided intervention. *Medical image analysis*, *12*(5), 577-585.

Wiles, A. D., Thompson, D. G., & Frantz, D. D. (2004, May). Accuracy assessment and interpretation for optical tracking systems. In *Medical Imaging 2004* (pp. 421-432). International Society for Optics and Photonics.